Reflectivity of the 410-km discontinuity from *PP* and *SS* precursors

K. Chambers
Department of Earth Sciences, University of Oxford, Oxford, UK

A. Deuss
Institute of Theoretical Geophysics, Department of Earth Sciences, University of Cambridge, Cambridge, UK

J. H. Woodhouse
Department of Earth Sciences, University of Oxford, Oxford, UK

Received 28 July 2004; revised 3 November 2004; accepted 18 November 2004; published 15 February 2005.

[1] A number of studies have confirmed the global existence of a transition zone discontinuity at 410 km depth by aligning large numbers of long-period seismograms on a surface reflection phase before stacking. In particular, *SS* and *PP* precursors from the 410-km discontinuity (termed *P*410*P* and *S*410*S*) have revealed long-wavelength topography of this discontinuity. Here we extend these techniques to examine the reflection coefficient of the 410-km discontinuity. Using our measurements of *P*410*P* and *S*410*S* amplitudes, we constrain the impedance contrasts across the 410-km discontinuity. We also show lateral variations in the *P* wave impedance contrast at 410 km, which is typically low under North America and China and higher beneath the North Pacific. The *S* wave impedance contrast shows less variability on the regional scale. However, analysis of *P*410*P* and *S*410*S* amplitudes over smaller areas (by binning traces into spherical caps) shows that the *S* wave reflection coefficient varies over much shorter scale lengths than that for *P* waves. The different patterns of variation for *P*410*P* and *S*410*S* reflection amplitudes could be due to the presence of melt, water, or other chemical heterogeneities in the transition zone. Other factors such as temperature or mantle olivine content variations could also influence precursor amplitudes, but they would be expected to lead to correlated variations, and so they cannot explain all the variation that we observe.

Citation: Chambers, K., A. Deuss, and J. H. Woodhouse (2005), Reflectivity of the 410-km discontinuity from *PP* and *SS* precursors, *J. Geophys. Res.*, *110*, B02301, doi:10.1029/2004JB003345.

1. Introduction

1.1. Background

[2] Discontinuous jumps in seismic properties result in refracted, reflected, and converted phases. Seismologists have used the phases resulting from interactions with discontinuities to study changes in mantle properties. Mantle discontinuities at 410 and 660 km depths subdivide the mantle into the upper mantle, transition zone, and lower mantle. The presence of these discontinuities on a global scale has long been established, and their inclusion in one-dimensional velocity models such as PREM [*Dziewonski and Anderson*, 1981] is largely undisputed.

[3] The discontinuities at 410 and 660 km are believed to be the result of polymorphic phase transformations in olivine (for a recent review, see *Helffrich* [2000]). At around 410 km depth, α-olivine transforms to β-wadsleyite, and around 660 km depth, γ-ringwoodite decomposes into magnesio-wüstite, (Mg, Fe)SiO_3, and perovskite, (Mg, Fe)O. In addition, a discontinuity at approximately 520 km depth has been identified by a number of studies [*Shearer*, 1996; *Flanagan and Shearer*, 1998; *Deuss and Woodhouse*, 2001], which is associated with the change of wadsleyite to ringwoodite. Lateral variations in mantle temperatures, in accordance with the reaction's Clapeyron slope, are expected to create a depth dependence for the resulting mantle discontinuities. So, in principle, topography of the 410-km discontinuity provides seismologists with a tool for measuring lateral temperature variations in the mantle.

[4] The amplitude of scattered waves from a discontinuity also provides information on the discontinuity thickness and the contrast in elastic parameters across the boundary. Current measurements of the reflection coefficient and impedance contrast of the 410-km discontinuity are limited to regional studies [*Revenaugh and Jordan*, 1991; *Vidale and Benz*, 1992; *Revenaugh and Sipkin*, 1994a; *Rost and Weber*, 2002; *van der Meijde et al.*, 2003] or global average measurements [*Shearer*, 1996; *Shearer and Flanagan*, 1999].

[5] Here we analyze precursors to the *PP* and the *SS* phase recorded on long-period seismograms, focusing dis-

0148-0227/05/2004JB003345$09.00

cussion on the arrivals corresponding to underside reflections from the 410-km discontinuity (*P*410*P* and *S*410*S*). We begin by examining stacks which image discontinuity structure in our global data set and in broad regions. In particular, we show lateral variations in *P*410*P* and *S*410*S* reflection amplitudes beneath Eurasia, the northern Pacific, and North America, which we interpret as variations in the impedance contrast across the discontinuity. We then examine precursor amplitude variations on a global scale by making stacks for spherical caps. Knowledge of the global variation in reflection amplitudes from the 410-km discontinuity can provide important answers to problems in mantle dynamics such as the amount and extent of variation in mantle's olivine content and the distribution of water as well as other chemical and thermal heterogeneities.

1.2. The 410-km Discontinuity by Precursor Studies

[6] Underside reflections from discontinuities (i.e., *PdP* and *SdS*, where *d* is reflection depth, Figure 1) provide a powerful method to study mantle discontinuities on a global scale as the point of interaction between the seismic wave and the discontinuity is halfway between the source and receiver (the bounce point). This means precursor studies are less constrained than other methods by the uneven distribution of sources and receivers. This paper will focus on the observation of underside reflections from the 410-km discontinuity (*P*410*P* and *S*410*S*).

[7] *Neele and Snieder* [1992] and *Neele et al.* [1997] have shown that *PdP* and *SdS* phases have a complicated travel time surface near the bounce point that can lead to interference from out of plane reflections and errors in determination of discontinuity depth. Despite this, the technique still remains the most effective method for large-scale (>1000 km) mapping of upper mantle and transition zone discontinuities.

[8] Much previous work has focused on precursors to the *SS* phase [e.g., *Shearer*, 1993; *Gossler and Kind*, 1996; *Flanagan and Shearer*, 1998; *Gu et al.*, 1998]. These studies have restricted discussion to long-wavelength transition zone discontinuity topography and its implications for lateral variations of transition zone temperatures. *PP* precursors have also been used to study the topography of the 410-km discontinuity [*Flanagan and Shearer*, 1999] and to constrain the properties of the 660-km discontinuity [*Estabrook and Kind*, 1996; *Shearer and Flanagan*, 1999; *Rost and Weber*, 2002]. *Shearer and Flanagan* [1999] used a comparison of *PP* and *SS* precursor amplitudes to constrain the seismic velocity and density jumps across the discontinuity. Here we use similar methods to search for lateral variations in the 410-km discontinuity position and reflection amplitudes using both *P* and *S* wave reflected phases.

1.3. Amplitude of 410 Reflections: Thickness Versus Impedance Contrast

[9] Reflection amplitudes are influenced by many factors including, the discontinuity thickness and impedance contrast, intrinsic attenuation, mantle structure, and anisotropy, all of which are complex functions of the Earth's thermal and chemical state. The goal of any study of reflected amplitudes is to minimize the contribution of the latter three, allowing interpretation in terms of the discontinuity properties. Variations in reflection amplitudes observed with short-period data have been primarily interpreted as changes in discontinuity thickness while variations observed using long-period data are more likely to be due to changes in impedance contrast.

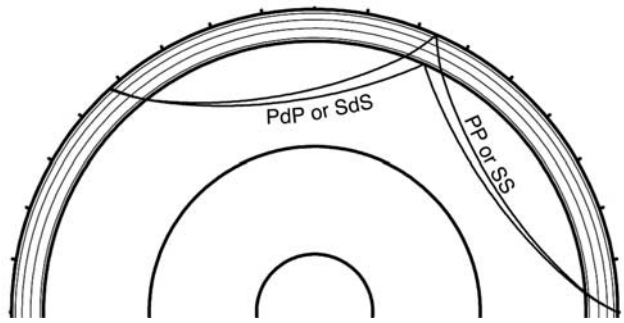

Figure 1. Ray paths for a reference phase (*PP* or *SS*) which reflects at the surface halfway between the source and receiver (bounce point). The precursor phase (*PdP* or *SdS*) reflects off the underside of a discontinuity at depth, *d*. The time lag between the precursor and the reference phase can be used to measure discontinuity depth and the relative amplitude of the precursor is a measure of the reflection coefficient.

[10] *Vidale and Benz* [1992] observed a high-frequency reflection from the 410-km discontinuity as a precursor to the $P'P'$ phase. This restricted the possible width of the phase transition to ~4 km as reflected phases are only sensitive to impedance gradients less than one quarter wavelength. *Rost and Weber* [2002] studied transition zone discontinuities beneath the western Pacific, finding the 410-km discontinuity to be sharper than 6 km with a minimum impedance contrast of 6.5%. Recently, *van der Meijde et al.* [2003] examined receiver functions from the 410-km discontinuity under Europe finding the width of the 410-km discontinuity to be as much as 25–35 km. These measurements of discontinuity thickness are generally derived by comparison of the frequency dependence of observed amplitudes with those predicted using a linear impedance gradient. However, *Helffrich and Wood* [1996] have shown that 5-km linear impedance gradients can yield a reflection coefficient the same as that for a 10-km width transition which has a nonlinear impedance gradient. Since it seems more likely that the impedance gradient is nonlinear within the $\alpha - \beta$ olivine phase transition [*Stixrude*, 1997], this would suggest that the above estimates of discontinuity thickness are minima. The important point is that variation in reflected amplitudes observed in short-period data could be due to variation in discontinuity thickness, which is probably in the range 4–30 km.

[11] Variation in phase transition thickness is generally attributed to variations in mantle water content [*Helffrich and Wood*, 1996; *Helffrich*, 2000; *van der Meijde et al.*, 2003]. As water preferentially partitions into the wadsleyite phase by about 10:1 [*Wood*, 1995], the wadsleyite phase is stable at lower pressures in regions where there is more water. This results in a broadening of the region where both phases are stable in hydrous regions of the mantle.

[12] The only long-period observations of 410-km reflection variability are those derived from *ScS* reverberations [*Revenaugh and Jordan*, 1991; *Revenaugh and Sipkin*, 1994a; *Gaherty et al.*, 1999]. These are in many ways

Table 1. Data Selection Parameters for the *PP* and *SS* Data Sets

Data Set (Reference Phase)	*PP*	*SS*
Components	vertical	horizontal
Event date range	1990–1999	1990–1999
Event size m_w	5.5–6.5	6.0–7.0
Number of events	2425	796
Time range from reference phase,[a] s	−270 to +90	−700 to +300
Epicentral distance, deg	80–140	100–160

[a]The time ranges were taken relative to the expected arrival times of the reference phase in PREM.

similar to the *S*410*S* reflections studied here; however, observation is restricted to regional corridors between sources and receivers. *Revenaugh and Sipkin* [1994a, 1994b] examined *ScS* reverberations between events in Japan and stations in China. They found the 410-km reflection coefficient for *S* waves to be increased under northwestern China and Mongolia. These long-period *ScS* studies utilized data with a cutoff frequency of 25 mHz; this equates to minimum effective wavelength of ∼194 km at 410 km depth. This suggests that the reflection amplitude variations observed by *Revenaugh and Sipkin* [1994a] are more likely to be due to changes in the impedance contrast of the discontinuity than to variations in discontinuity thickness.

2. Data Processing and Analysis

2.1. Data Selection

[13] We used broadband data sampled at 1 s from the Incorporated Research Institutions for Seismology/International Deployment of Accelerometers/U.S. Geological Survey (IRIS/IDA/USGS) network. Our selection criteria for the two data sets (referred to by their reference phase as *PP* or *SS*) are shown in Table 1. We use records from shallow events (<75 km) to minimize interference from depth phases. The epicentral distance intervals were chosen to maximize underside reflections from the upper mantle and transition zone discontinuities while minimizing the interference from other phases. Figure 2 shows the global distribution of *PP* and *SS* source-receiver midpoints (bounce points). For both data sets, coverage is best in the North Pacific, and for the *PP* data this extends into China and northern Asia.

[14] The data were Butterworth band-pass filtered (power of 6) between 8 s and 75 s for *PP* and 15 s and 75 s for *SS*. The records were also deconvolved for long-period instrument response. A Hilbert transform was applied to the *PP* data, and the *SS* data were rotated to obtain the transverse component.

2.2. Stacking Method

[15] We enhance arrivals with amplitudes below the noise level of individual records by stacking large numbers of traces in the time-slowness domain. By selecting records that have bounce points in certain regions, it is possible to look at possible lateral variations in discontinuity properties. However, as stacked trace quality increases with the number of traces in the stack, there exists a trade-off between lateral resolution and stack accuracy.

[16] The initial (predeconvolution) stacking procedure is similar to previous precursor studies [*Flanagan and Shearer*, 1998; *Gu et al.*, 1998; *Flanagan and Shearer*, 1999; *Deuss and Woodhouse*, 2002]. In addition to these techniques we select and align our data on the basis of the cross correlation of the trace with an existing reference pulse, and we remove the sea surface reflection from the *PP* pulse (see procedure 6). A summary of the stacking procedure is as follows:

[17] 1. We produced average *PP* and *SS* reference pulses by stacking ∼1000 handpicked seismograms. These were selected for the clarity of their *PP* or *SS* waveforms and were aligned on their maxima before stacking.

[18] 2. We then select data sets by cross correlating the filtered seismograms with the average reference pulses. Only data with a correlation coefficient $\geq$0.6 and signal-to-noise ratio greater than 3 are used. The signal-to-noise ratio was measured as the ratio of energy in the window (60 s for *PP*, 100 s for *SS*) containing the reference phase to that in the window prior to the reference phase.

[19] 3. The arrival time of the surface reflection is measured for each selected trace using the absolute maximum of the cross-correlation function within time widows of 16 s for *PP* and 32 s for *SS* around the expected arrival time of the reference phase (from PREM). The sign of the cross-correlation maximum was used to determine the traces polarity, which was corrected before stacking.

[20] 4. The surface reflection energy was determined over time windows of 60 s around the *PP* pulse and 100 s around *SS*. This was used to normalize the trace before stacking to prevent large events dominating the stack. In addition, the stacks were weighted by the record's signal-to-noise ratio.

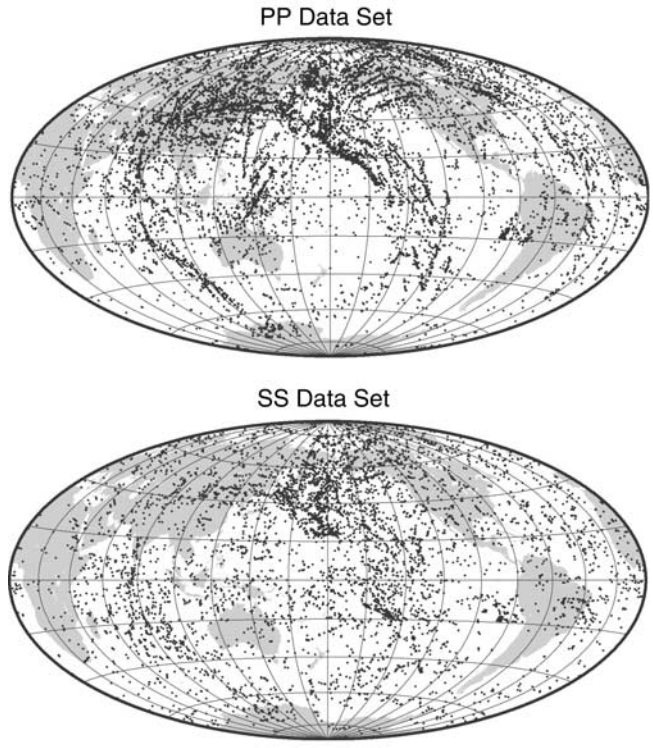

Figure 2. Locations of the bounce points (source-receiver mid points) for the traces used in the *PP* and *SS* data sets. Our final data sets contain 10,627 and 6138 traces, respectively, for the *PP* and *SS* data sets.

[21] 5. The expected reflection amplitudes were determined, using WKBJ synthetic seismograms [*Chapman*, 1978] for PREM and applying the same filters as our data for our range of epicentral distances. The amplitudes of the precursor section of each trace were corrected for distance effects using the ratio of the expected reflection amplitudes in the trace to that at the reference distance.

[22] 6. For the *PP* data with oceanic bounce points the effect of the ocean (ocean function) was removed from the reference phase section of the trace. The ocean function is estimated as two spikes representing *P* wave reflections from the ocean floor and surface. The spike amplitudes were obtained by deconvolving an oceanic *PP* pulse (obtained by stacking records with oceanic bounce points) with a continental *PP* pulse (obtained from a stack of records with continental bounce points). The spike separation was calculated using the local ocean depth in ETOPO5 [*National Oceanic and Atmospheric Administration* (*NOAA*), 1988]. Crustal reverberations near the bounce point also distort the reference phases; however, tests with WKBJ synthetics showed the effect of this on our measurement of precursor amplitudes is minor.

[23] 7. Data are aligned on the arrival time of the surface reflection and stacked in the time slowness domain. Each trace in the stack is time shifted by $(\Delta - \Delta_r)$ times the slowness (relative to the reference phase), where Δ is the epicentral distance and Δ_r is a reference distance (110° for *PP* 130° for *SS*). A summary stacked trace is made by taking a profile through the time-slowness stack along the expected arrival time and slowness of precursor phases in PREM.

[24] 8. To assist interpretation, stacked traces are deconvolved (see section 2.3) and converted to depth on the basis of the expected arrival time of precursor phases in PREM [*Dziewonski and Anderson*, 1981]. Before depth conversion we apply travel time corrections for crust and mantle structure using CRUST5.1 and S20RTS [*Mooney et al.*, 1998; *Ritsema et al.*, 1999].

2.3. Accurate Measurement of Precursor Arrival Time and Amplitude

[25] We separate out arrivals in the stacked trace using an iterative deconvolution technique similar to that first used by *Kikuchi and Kanamori* [1982] and subsequently extended by *Bona and Boatwright* [1991].

[26] The trace, d_m, is modeled as a convolution of the surface reflection (or reference pulse), g_m, with a reflectivity sequence (or deconvolved trace), r_n:

$$d_m = \sum_n g_{m-n} r_n \tag{1}$$

Equation (1) can be represented in matrix form:

$$\mathbf{d} = \mathbf{G}\mathbf{r} \tag{2}$$

where the trace vector $\mathbf{d}$ is obtained by multiplying the reflectivity sequence vector $\mathbf{r}$ by the matrix $\mathbf{G}$. The columns of $\mathbf{G}$ will be the reference pulse with a delay appropriate to the corresponding element of $\mathbf{r}$. In principle, it is possible to obtain a deconvolved reflectivity sequence directly by multiplying the data trace by the generalized inverse operator $\mathbf{G}^{-\mathbf{g}}$ [*Menke*, 1989]:

$$\mathbf{r} = \mathbf{G}^{-\mathbf{g}}\mathbf{d} \tag{3}$$

However, in practice, best results are obtained by applying equation (3), with a limited number of positions for reflection coefficients rather than parameterizing each time sample as a potential reflector.

[27] We determine the spike positions in the deconvolved trace by cross correlating the reference pulse with the trace. The spike position is placed at the maximum, and its amplitude is calculated using equation (3). We then derive a model trace by convolving the reference pulse with the spike sequence. This model trace is subtracted from the data trace before subsequent cross correlation with the reference pulse to determine the next spike position. At each step all the reflection coefficients are solved for simultaneously, and the fit of the model trace to the data is measured using an *F* test on the variance. The process continues until the addition of a spike in the reflectivity sequence fails to improve the fit of the model trace to the data by more than 0.1%.

2.4. Uncertainty in Precursor Amplitude and Arrival Time

[28] We determine the errors in our stacks using a bootstrap resampling procedure [*Efron and Tibshirani*, 1991]. For the predeconvolution data stacks the process is straightforward. A bootstrap distribution for each time sample of the stacked trace is derived by making repeated stacks (500) using traces from the original population, randomly selected with replacement. We then estimate the error on the amplitude of each time sample from the standard deviation of the bootstrap distribution.

[29] The application of the nonlinear deconvolution operator complicates the estimation of the error in the deconvolved stacks. When the deconvolution operator is applied to traces made from bootstrap samples, the position of an arrival will vary, leading to an overestimate of amplitude error at a given time sample if a straightforward bootstrap is applied. To obtain the true bootstrap distribution for the amplitude of an arrival, it is necessary to sum the amplitudes over a time window. The window width is determined by the range for which a discontinuity is seen in the bootstrap samples. Similarly the mean and standard deviation of the arrival time can be calculated from the frequency distribution of the arrival times in the bootstrap data.

[30] In cases where arrivals in the deconvolved trace are well constrained the technique works well. However, where the data is less robust the arrival positions in the bootstrap stacks can vary greatly which can result in the arrival windows for adjacent reflections overlapping. This makes the method unsuitable for noisy/less reliable stacked traces; in these cases it is only possible to measure *P*410*P* and *S*410*S* amplitudes from the deconvolved mean trace.

3. Regional Stack Results

3.1. General Discontinuity Observations

[31] We begin by making stacks of all the traces in our *PP* and *SS* data sets, and stacks which include traces with bounce points in the four regions shown in Figure 3. These

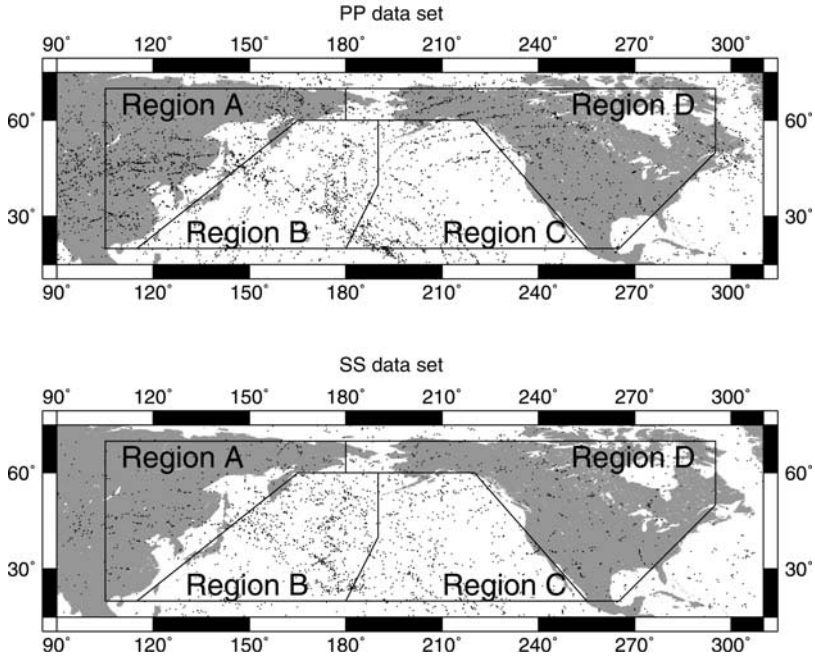

Figure 3. Locations of the *PP* and *SS* bounce points together with outlines of the regions used to make the stacks in Figure 4. Regions A, B, C, and D contain 2105, 1340, 1197, and 1355 *PP* traces and 611, 1026, 838, and 691 *SS* traces, respectively.

regions were chosen to maximize the number of seismograms and hence stacked trace quality without averaging out lateral variability. Figures 4a and 4b show the resulting stacked traces. In each stacked trace, precursor phases are visible arriving prior to the reference pulse, which is aligned at zero time. We also show WKBJ synthetic seismograms computed using PREM, for the same source-receiver geometries as the data. The results of deconvolution and depth mapping of the stacked traces are shown in C and D. The arrival from the 410-km discontinuity is the most robust and the largest feature of the two data sets, arriving ~80s and ~150s prior to the *PP* and *SS* phases, respectively. Discussion of the lateral variations of the 410-km discontinuity will be the focus of the remaining sections of this paper, here we briefly mention some of the other discontinuities observable in the stacks.

[32] Several of the stacks show the possible presence of upper mantle discontinuities, arrivals from a 220-km discontinuity are observed in the northwest Pacific and North America, although the later is not picked out by the deconvolution. These arrivals are of much smaller amplitude than those predicted by PREM synthetics. The North Pacific (regions B and C) for *PP*, and all of the regions for *SS*, show arrivals consistent with a reflector at approximately 300 km depth (arriving at ~−70 s for *PP*, and ~−125 s for *SS*). This arrival is small and could be attributed to a sidelobe of the *P*410*P* and *S*410*S* phases. However, both *Revenaugh and Sipkin* [1994a] and *Deuss and Woodhouse* [2002] have also made observations of a discontinuity at this depth using long-period *S* waves.

[33] Examination of the predeconvolution stacks shows that the sidelobe of the 410-km reflection ~100s and ~175s prior to the *PP* and *SS* is much larger than its counterpart in the reference pulse. The deconvolution algorithm separates out this sidelobe, which is consistent with a reflection from a 520-km discontinuity. We also observe splitting of the 520-km discontinuity in the *SS* precursor stack for North America (region D), and to a lesser extent in the North Pacific, consistent with the observations of *Deuss and Woodhouse* [2001]. A 660-km reflector is consistently observed in the *SS* data, while it is not observed in *PP*. Although the deconvolution algorithm picks out *P* arrivals consistent with reflections from 600–700 km depth these show a wide range of depths, and are inconsistently observed.

3.2. Variation in Reflection Amplitudes From the 410-km Discontinuity

[34] We now focus on the reflections from the 410-km discontinuity. To demonstrate the variability of the 410 reflection amplitudes in our regional stacks, we show frequency histograms for the *P*410*P* and *S*410*S* amplitudes measured in 1000 bootstrap samples (Figure 5). The *PP* data set shows that the amplitude of the *P*410*P* phase is slightly lower than the global stack when measured under the continental regions (A and D) and higher beneath oceanic regions (B and C). The *SS* data set shows a different pattern. The mean amplitudes of regions B, C and D are similar for *SS* while region A shows a higher mean amplitude and larger variance.

[35] The amplitudes of *P*410*P* and *S*410*S* in the global stacks are slightly lower than those of *Shearer and Flanagan* [1999]. This could be due to differences in the way amplitudes are measured between the two studies or our use of data with shorter periods, which results in less coherent stacking due to discontinuity topography and velocity heterogeneities.

[36] In order to interpret our observations of *P*410*P* and *S*410*S* in terms of changes in the discontinuity properties it is necessary to exclude the possibility that the ampli-

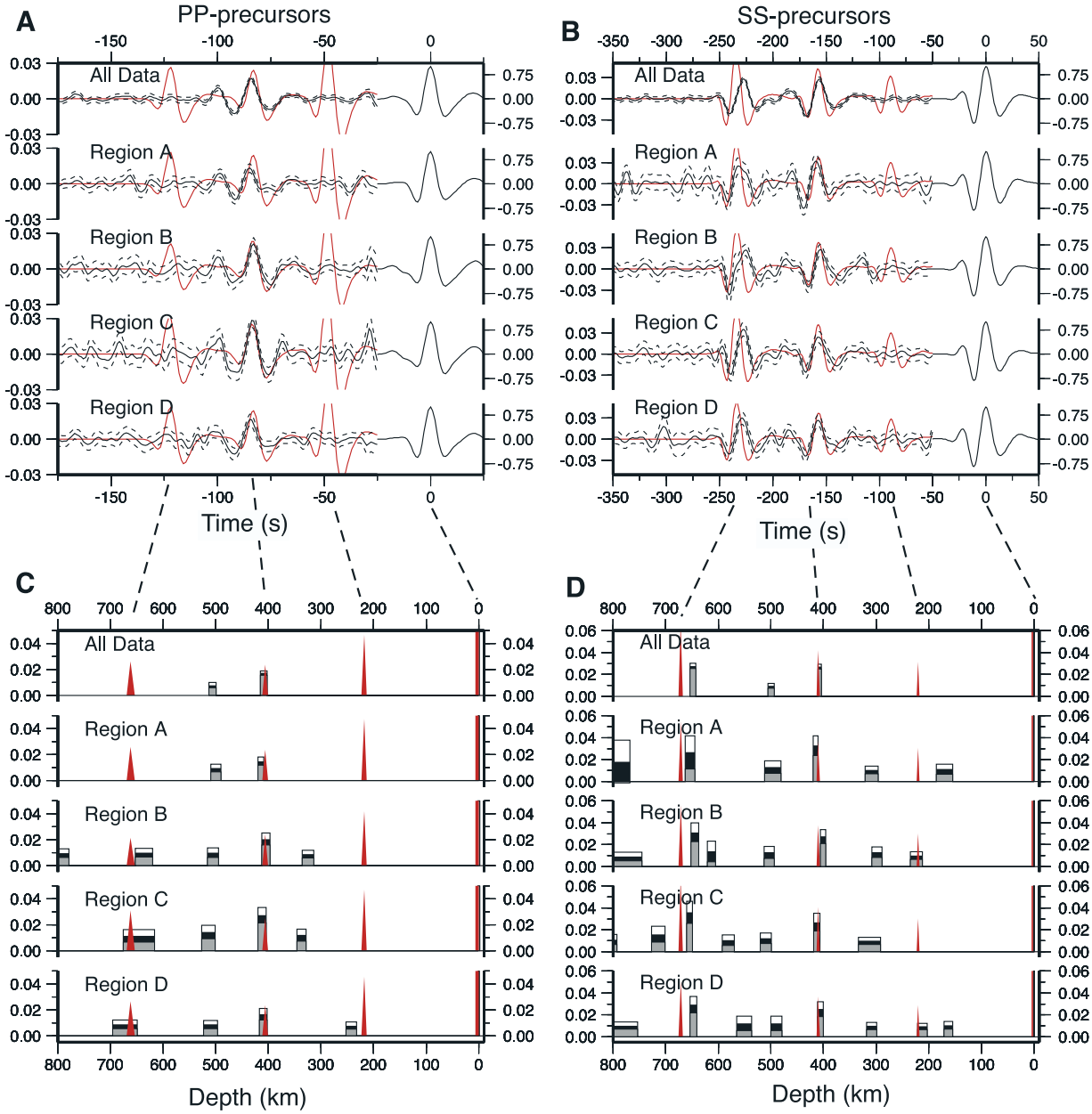

Figure 4. Resulting stacks for the whole data set and the four regions showing (a) *PP* and (b) *SS* precursor phases. Dashed lines represent the 95% confidence limits for the stack determined by bootstrap resampling. The red line shows stacks of the synthetic seismograms which incorporate the reference phase and reflections from 220, 410, and 660 km depth. and Results of the bootstrap analysis on the deconvolved stacks. Depth mapping for (c) *PP* and (d) *SS* precursors. The black bar shows the mean amplitude, while the gray and white represent the 95% confidence limits. Bar width represents the uncertainty in discontinuity depth. Red spikes show the deconvolution results for the WKBJ synthetics.

tudes are biased by the presence of other phases. Record sections such as those of *Flanagan and Shearer* [1998, 1999] show that there are no interfering phases of significant amplitude that arrive coincident with *S*410*S* at 130°. Similar sections for *PP* precursors show there is a possibility of interference from *PKP* at around 125°. However, the range of offset distances used here, and the procedure of stacking in the time-slowness domain, means that the contribution from other phases to the precursor amplitudes is minimal.

[37] It is possible that the presence of velocity heterogeneity could focus or defocus rays and result in amplitude variations. However, heterogeneity located away from bounce point would affect precursor and surface reflection equally, and so would not change the amplitude of the precursor phases which is always measured relative to the

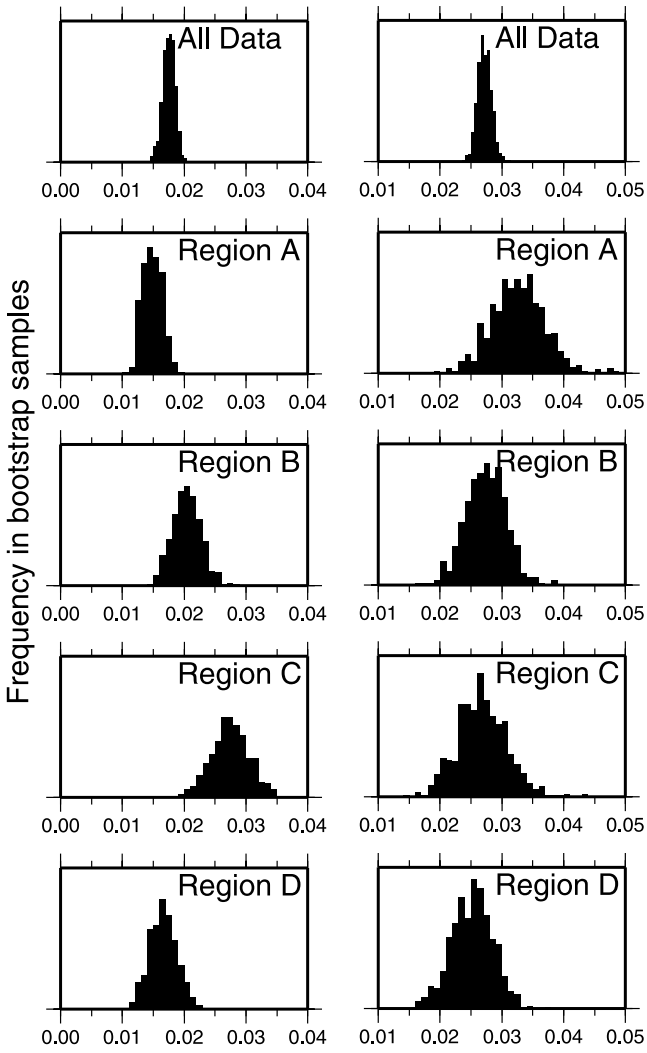

Figure 5. Distribution of (left) *P*410*P* and (right) *S*410*S* amplitudes measured in 1000 bootstrap samples made for each of the regional stacks.

surface reflection. Focusing due to structure between the discontinuity and the bounce point would be expected to affect the *PP* and *SS* data sets equally as they have the same effective wavelength.

[38] A similar argument is true for the focusing due to discontinuity structure, which has been shown to affect precursor amplitudes in individual records by *Neele and Snieder* [1992]. Incoherent stacking also reduces the potential amplitude of precursor phases (see section 3.3); however, this will also affect *P*410*P* and *S*410*S* equally due their similar wavelengths. We do not see similar variation in *P*410*P* and *S*410*S* amplitudes, so the variations in amplitude that we observe must be due the properties of the discontinuity rather than focusing effects.

[39] The main factors which affect the *P*410*P* and *S*410*S* amplitudes are impedance contrast and discontinuity thickness. Previously the 410-km discontinuity has been modeled by an impedance gradient ranging between 4 and 30 km in length [*Vidale and Benz*, 1992; *Rost and Weber*, 2002; *Helffrich and Wood*, 1996; *van der Meijde et al.*, 2003]. These lengths are all shorter than one quarter of the peak wavelength of our data (~38 km). Accordingly, the long-period data used here will not be sensitive to changes in discontinuity thickness. Thus variations in *P*410*P* and *S*410*S* amplitudes are most easily explained by changes in the impedance contrast across the 410-km discontinuity.

3.3. Impedance Contrast at 410 km

[40] To investigate the lateral variations in *P*410*P* and *S*410*S* amplitudes, we employ a grid search method to establish the combination of *S* wave and *P* wave impedance contrasts that best match the data. Because the precursor amplitudes are corrected for differences in epicentral distance, the amplitude for the 410-km phases in the deconvolved trace can be considered a measure of the reflection coefficient at the stack reference distance. Formulae for calculating the reflection amplitude from contrasts in seismic velocity and density are given by *Aki and Richards* [1980]. Using the PREM values for seismic velocity and density above the 410-km discontinuity, with ray parameters corresponding to the reference distances, we calculated reflection coefficients for *P*410*P* and *S*410*S* phases for a range of density and seismic velocity jumps across the boundary. We then calculated the squared misfit between the theoretical reflection amplitudes and our measured *P*410*P* and *S*410*S* amplitudes (Figure 6).

[41] Trade-offs exist between density and seismic velocity changes when modeling reflection amplitudes in this way. So, it is more useful to interpret the results in terms of impedance contrasts. Here we refer to impedance contrast as the fractional change in impedance across the boundary $\frac{\Delta z}{z_1}$.

$$\frac{\Delta z}{z_1} = \frac{z_2 - z_1}{z_1} = \frac{v_2 - v_1}{v_1} + \frac{\rho_2 - \rho_1}{\rho_1} \tag{4}$$

Where seismic impedance is given by the product of seismic velocity and density ($z = \rho v$), and the subscripts refer to material properties on either side of the boundary.

[42] Differences in crust/mantle structure and discontinuity topography can cause misalignment of the precursor phases in the stacking process and result in lower amplitudes. We attempt to compensate for this effect by assuming that the precursor arrival times in a stack have a Gaussian distribution with standard deviation σ. Determination of σ is difficult and a true value will depend on the region covered by the stack. *Shearer* [1996] and *Shearer and Flanagan* [1999] used 1.7 s for *PP* and 2.5 s for *SS*, while *Revenaugh and Jordan* [1991] found σ to be 3.0 ± 1.0 s for ScS_{660} reverberations. We determine σ of 2.3 and 3.4 s for *P*410*P* and *S*410*S*, respectively, by examining the uncorrected *P*410*P*-*PP* and *S*410*S*-*SS* lag times in stacks for spherical caps of 10° radius. These are greater than the values used by *Shearer* [1996] and *Shearer and Flanagan* [1999]; however, our values are derived from a global distribution of stacks rather than just traces with oceanic bounce points. We convert these σ into correction factors for our measured amplitudes by convolving the relevant reference phases with the appropriate Gaussian distribution, and then deconvolve this signal using the original reference phase. Our values for σ result in correction factors of 0.66 and 0.72 for *P*410*P* and *S*410*S*.

[43] The application of a single fixed correction factor to the global and regional stacks assumes that discontinuity

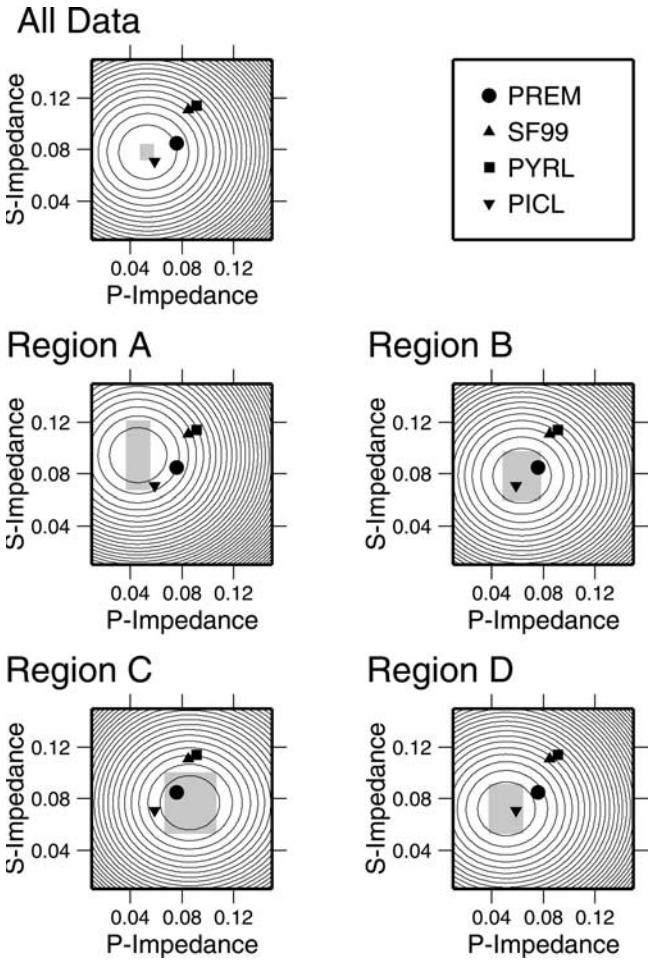

Figure 6. Grid search results for the impedance contrast at 410 km for all data and the four regions. Contours show squared misfit to the measured 410-km amplitudes. The shaded region refers to models which result in *P*410*P* and *S*410*S* amplitudes with in the range of our observations. For reference we also show the models of *Shearer and Flanagan* [1999] (SF99) and PREM [*Dziewonski and Anderson*, 1981]. Expected impedance contrasts for the pyrolite (PYRL) and piclogite (PICL) models determined from *Shearer and Flanagan* [1999] are also shown.

topography and velocity heterogeneity within the regions is similar to the global average. Given the broad regions used in this study, this assumption seems satisfactory; however, application of the factors to smaller areas could lead to overestimates of the impedance contrast.

[44] Using the grid search (Figure 6), we constrain the *P* wave and *S* wave impedance contrasts across the 410-km discontinuity for our global and regional stacks. The best fitting values with their errors are given in Table 2; for comparison we also give the results from previous studies in Table 3. The optimum model of *Shearer and Flanagan* [1999] has higher *P* and *S* wave impedance contrasts than we measure. This is not surprising, as *Shearer and Flanagan* [1999] measure higher amplitudes for *P*410*P* and *S*410*S* reflections than we do. However, *Shearer* [1996] measured similar *S*410*S* amplitudes to ours and arrived at a similar value for the *S* wave impedance contrast.

Table 2. Optimum Values for *P* Wave and *S* Wave Impedance Contrasts in the Global Stack and the Four Regions

	P Wave Impedance	*S* Wave Impedance
All data	0.053 ± 0.005	0.078 ± 0.006
Region A	0.046 ± 0.010	0.095 ± 0.027
Region B	0.064 ± 0.015	0.079 ± 0.019
Region C	0.087 ± 0.020	0.077 ± 0.024
Region D	0.051 ± 0.013	0.072 ± 0.019

[45] *Revenaugh and Sipkin* [1994a] found normal incidence *S* wave reflection coefficients of 0.032 around Japan and south China and 0.066 in northern China. The normal incidence *S* wave reflection coefficient for our study region A (0.044 ± 0.014) is consistent with the average of these values. *Gaherty et al.* [1999] require that the vertical incidence *S* wave reflection coefficient at the 410-km discontinuity lies between 0.03 and 0.055; the value determined from our global stack lies within this range at 0.038 ± 0.004.

[46] Our measurements of global *P* wave impedance contrast are lower than previous studies global studies such as *Shearer and Flanagan* [1999], although their 95% confidence limits include values as low as 0.06. The value for the northwest Pacific determined by *Rost and Weber* [2002] (0.065) is within the range of the comparable regions B and C. However, our global stack and regions A and D all show lower *P* wave impedance contrasts than previous studies. This could be due to differences in bounce point distribution or to an underestimation of the incoherent stacking correction factor in regions with large variations in discontinuity topography and or upper mantle heterogeneity.

4. The 410-km Reflection Amplitudes on a Global Scale

4.1. Discontinuity Structure of the Study Regions

[47] We examine the discontinuity topography and reflection amplitudes from 410 km by making stacked traces for equally spaced overlapping spherical caps. In a similar fashion to previous studies of discontinuity topography [*Flanagan and Shearer*, 1998; *Gu et al.*, 1998; *Flanagan and Shearer*, 1999], we divide the Earth into 410 equally spaced caps and then make stacks of all traces with bounce points within 10° of each cap center.

Table 3. Results of Previous Studies for *P* Wave and *S* Wave Impedance Contrasts at 410 km

	P Wave Impedance	*S* Wave Impedance
Revenaugh and Jordan [1991]	-	0.046 ± 0.01
Shearer [1996]	-	0.067 ± 0.011
Shearer and Flanagan [1999] (optimum)	0.085	0.111
Gaherty et al. [1999]	-	0.092 ± 0.03
Rost and Weber [2002]	0.065	-
PREM [*Dziewonski and Anderson*, 1981]	0.077	0.085
Pyrolite (∼65% olivine)[a]	0.0913	0.1138
Piclogite (∼40% olivine)[a]	0.0590	0.0705

[a]Expected impedance contrasts for pyrolite and piclogite mantles were adapted from *Shearer and Flanagan* [1999].

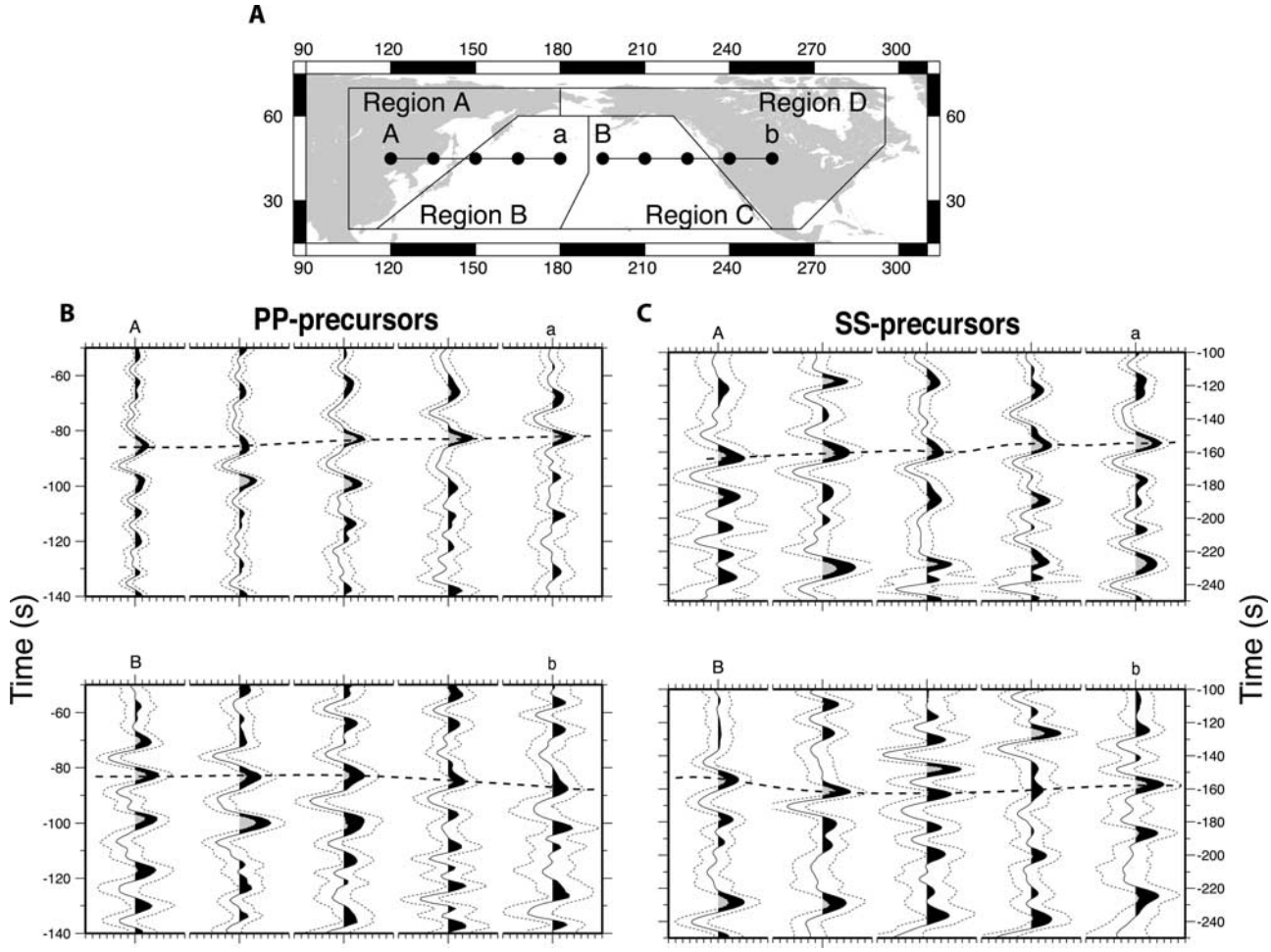

Figure 7. Stack track traces for 10 adjacent spherical caps. (a) Location of the caps with respect to the study regions. (b) *PP* and (c) *SS* precursors. The position of the 410-km arrival is marked with a thick dashed line while thin lines show the 95% confidence limits for the stacked traces. Stack amplitude is given relative to the reference phase with scale intervals of 0.01. The large negative swing prior to some of the *P*410 and *S*410*S* arrivals is presumably due to interference between reflections from 410 and 520 km depth.

[48] Figure 7 also shows that *P*410*P* amplitudes in regions B and C are greater, as was previously observed in the regional stacks. The *S*410*S* amplitudes show less systematic variation. In Figure 8 we present deconvolved depth-converted versions of the stacked traces. These reflectivity sequences also show discontinuity topography, notably both the *PP* and *SS* data sets show that the 410-km discontinuity is elevated under the eastern Pacific and depressed under China.

4.2. Global Variation in Reflectivity of the 410-km Discontinuity

[49] Figure 9 shows global maps for the amplitudes of *P*410*P* and *S*410*S* with a horizontal section through global *S* wave velocity perturbation model S20RTS [*Ritsema et al.*, 1999] at 410 km depth. For our reflection amplitude maps we emphasize the long-wavelength structure and reduce the dependence of results on individual caps by expanding the amplitude surface using degree-12 spherical harmonics. The harmonic coefficients were determined by least squares inversion. Gaps in the data coverage required regularization of the inverse problem. Tests showed that stable results were achieved by adding 0.1% of the average diagonal value to the inner product matrix. In addition we weight the data by the square root of the number of traces in each cap.

[50] We also compare our individual observations with local *S* wave velocity perturbations (Figure 10). There appears to be little correlation between the global patterns of *P*410*P* and *S*410*S* amplitudes. Examination of the amplitude maps suggests that *P*410*P* amplitudes are dominated by a long-wavelength pattern, Eurasian and North American amplitudes are low while Pacific amplitudes are high. *S*410*S* amplitudes appear to be dominated by a higher-degree pattern.

[51] To demonstrate the difference in scale length between *P*410*P* and *S*410*S* anomalies, we show power spectra for the two spherical harmonic expansions in Figure 11. The *P*410*P* spectrum is dominated by the degree-1 signature, while the *S*410*S* has only a small contribution from degree 1. The contributions to the *P*410*P* power spectra from the higher degrees are relatively uniform with slight decrease after degree 10. In contrast the *S*410*S* power spectrum is

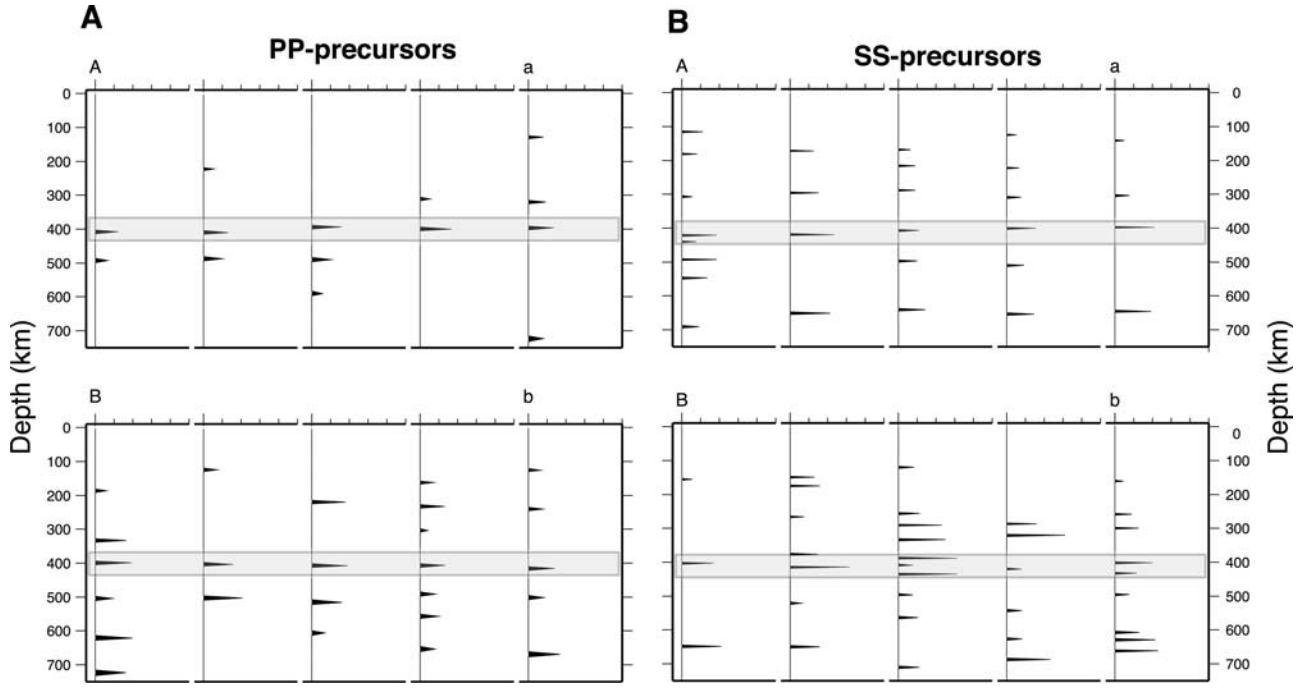

Figure 8. Deconvolved and depth converted stacked traces from Figure 7 for (a) *PP* and (b) *SS* precursor data. The region of the 410-km arrival is highlighted in each cross section. Amplitude scale is the same as Figure 7.

dominated by higher degrees, the peak contributions being from degrees 4 and 10. There is no significant decrease in the *S*410*S* power spectrum at higher degrees suggesting that degree-12 spherical harmonics are not sufficient to represent the amount of variation in *S*410*S* amplitudes we observe.

[52] Many of the regions of very high or low *S*410*S* amplitudes contain cap values which show considerable scatter (e.g., western Pacific, North Atlantic) and could potentially be the results of localized focusing effects. However, this is unlikely, as the *PP* data set has the same effective wavelength and similar azimuthal distribution to the *SS*, so focusing effects should affect both equally. Fewer short-wavelength high-amplitude variations are observed in *P*410*P* amplitudes, suggesting that *S* wave impedance contrast at the 410-km discontinuity has a much shorter scale of lateral variation than that for *P* waves. It is also possible that high amplitude short-wavelength *S*410*S* anomalies could be due to differences in data quality. However, the short-wavelength *S*410*S* amplitude structures persist in well sampled areas such as the northern Pacific. Hence we believe that the cause of the differences in the patterns of *S*410*S* and *P*410*P* amplitudes is related to the *P* and *S* impedance contrasts at the discontinuity. Accordingly, the spatial scale of variations in *S* impedance contrast must be shorter than the corresponding length for *P* wave impedance contrast.

[53] Shorter scale lengths for *S* wave impedance contrast at 410 km could explain the lack of variation in the regional estimates of *S* wave impedance contrast (section 3.3). Figure 9 shows that the lateral variations in *S*410*S* amplitudes are considerably shorter than the dimensions of the regions used to make the stacks in Figure 4. Yet the *P* wave impedance contrasts vary on similar length scales to the regions used in section 3.3. So, the lateral differences in *P*410*P* amplitude became apparent in the regional stacks, while variations in *S*410*S* amplitude were averaged out in the stacking process.

5. Discussion

5.1. General Observations of Discontinuities

[54] In addition to underside reflections from a 410-km discontinuity we observe a variety of other reflections from other upper mantle discontinuities in the regional stacks (Figure 4). We observe weak reflections from depths of 220 km and 300 km, which are consistent with the Lehmann and X discontinuities [*Deuss and Woodhouse*, 2002]. The inconsistent observation of arrivals from 220 km suggests that this discontinuity is not a global feature and, when present, produces much smaller reflections than those predicted using PREM.

[55] In many of the regions we observe splitting of the 520-km discontinuity as did *Deuss and Woodhouse* [2001]. However, in contrast to findings of *Deuss and Woodhouse* [2001], region A (northern Asia) does not show splitting of the 520-km discontinuity, possibly due to the broad region over which our stack averages. We also see no apparent splitting in the *PP* data set which could be due to sampling differences, or it is possible that the phase transitions in the nonolivine mantle components, which are believed to cause the splitting, are more transparent to *P* waves.

[56] The observation of a clear *S*660*S* phase requires that the absence of the 660-km reflector in the *PP* data set cannot be due to discontinuity topography or focusing effects because the two data sets have the same effective wavelength. The lack of observation of a *P*660*P* reflection is in agreement with the conclusions of *Estabrook and Kind* [1996] and *Shearer and Flanagan* [1999] whereby the

660-km discontinuity has a *P* wave impedance contrast of virtually zero.

5.2. Regional Observations of 410-km Reflection Amplitudes and Impedance Contrast

[57] Seismology, geodesy, geochemistry, and mineral physics all constrain mantle composition and behavior. Here we have extended the contribution from seismology to include lateral variations in reflection coefficients and impedance contrasts for the 410-km discontinuity on a global scale.

[58] By making stacks which include traces with bounce points within certain regions we have shown that variations in precursor amplitudes are observable. These differences cannot be attributed to interference from other phases or to focusing effects from discontinuity topography. Given the frequency range of the data used in this study, we also reject variation in discontinuity thickness as a cause for our observations of precursor amplitude variation. Instead, we believe these lateral variations in reflection amplitude are best modeled as lateral variations in impedance contrast.

[59] We find that *P* wave impedance contrasts of the 410-km discontinuity are significantly higher beneath the North Pacific compared to Asia and North America. This may suggest that the differences between oceanic and continental mantle extend to the top of the transition zone; however, when we analyze *P*410*P* and *S*410*S* amplitudes in stacks for spherical caps, there is no clear ocean-continent difference. For example, South America and the Middle East both show high *P*410*P* amplitudes.

[60] Differences in *S* wave impedance are not as significant and show more scatter, which is suggestive of lateral variations in impedance contrast with shorter length scale. This is confirmed by examination of *P*410*P* and *S*410*S* amplitudes in stacks for spherical caps which shows that the scale length of variations observed *P* wave reflectivity from the 410 is much greater than that for *S* waves.

5.3. Consequences for Composition and Lateral Heterogeneity in the Mantle

[61] Our low values for the *P* and *S* wave impedance contrasts of the 410-km discontinuity might appear to be more consistent with a low-olivine piclogite model for mantle composition. However, the predicted impedance contrasts across the discontinuity in pyrolite and piclogite models assumes an anhydrous wadsleyite phase. There is currently a lack of experimental information on the elastic properties of hydrated wadsleyite with realistic iron contents. *Yusa and Inoue* [1997] have shown that the addition of water to pure Mg-wadsleyite can reduce the bulk modulus by 5–11%, and *Jacobsen et al.* [2004] have shown that the addition of 1% wt of water to an Fo_{90} ringwoodite can reduce *P* and *S* wave impedance by 5.8 and 7.6%, respectively. Thus, if hydrated wadsleyite in the mantle behaves in a similar fashion then a pyrolite

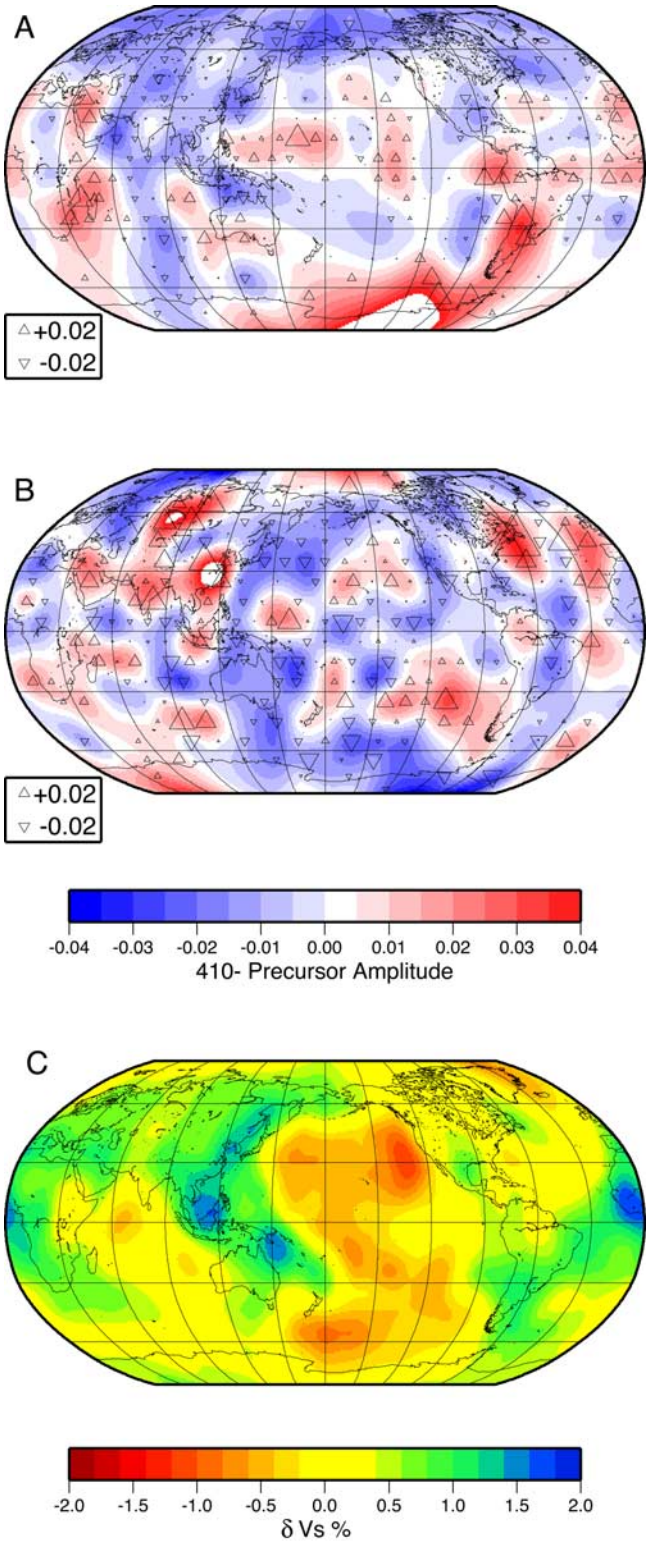

Figure 9. (a) *P*410*P* and (b) *S*410*S* reflection amplitudes. Triangles represent the amplitude difference from mean observed at each cap. Mean amplitudes are 0.032 for *P*410*P* and 0.047 for *S*410*S*. Colored contours represent the amplitude surface expanded in spherical harmonics to degree 12 and evaluated at the cap locations. (c) Section through mantle tomography model S20RTS [*Ritsema et al.*, 1999] taken at 410 km. For comparison with the amplitude variations, velocity anomalies were averaged over a 10 circle around each cap location. Data and spherical harmonic coefficients are available from ftp.earth.ox.ac.uk/pub/Kit/410/.

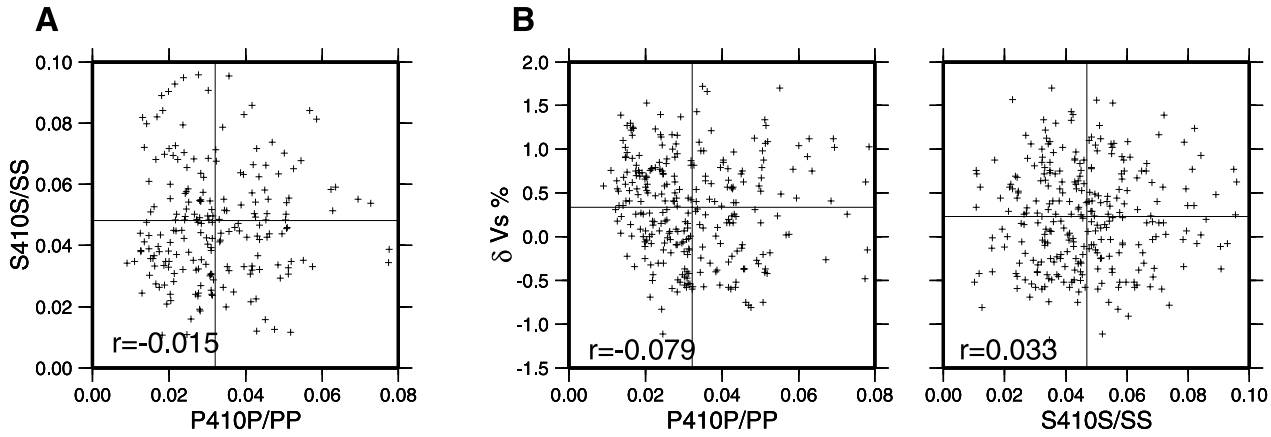

Figure 10. (a) Comparison of *P*410*P* and *S*410*S* amplitudes measured at each cap location. (b) Comparison of *P*410*P* and *S*410*S* amplitudes with velocity anomalies from tomography model S20RTS [*Ritsema et al.*, 1999] at 410 km depth. As in Figure 9, velocity anomalies were averaged over a 10° circle around the cap location. The product moment correlation coefficient (r) is shown for each pair of variables, and the cross is centered on the mean value for each axis.

mantle could still be consistent with our measured impedance contrasts of the 410-km discontinuity.

[62] The lack of correlation between *P* and *S* wave reflection amplitudes requires that mantle olivine content is not the major source of impedance variation for at least one of the data types. Other chemical variations, such as aluminium and iron content, are more likely to affect the width and depth of the phase transition [*Weidner and Wang*, 2000] rather than the impedance contrast and so are not likely to be the cause of the variations in precursor amplitude we observe.

[63] If lateral variations in mantle temperatures and their associated effects on elastic parameters were the cause of variations in 410-km impedance contrast, we would expect the variations in *P* and *S* wave reflection amplitudes to correlate. So it is not surprising that we also see no correlation between the measurements of precursor amplitude and velocity anomalies in S20RTS if these are taken as a proxy for lateral variations in temperature. Lateral differences in reflection coefficient will not be observed where a thermal anomaly is continuous across the discontinuity. As the $\alpha - \beta$ phase change and hence the 410-km discontinuity are believed to have a positive Clapeyron slope [*Helffrich*, 2000], this would aid the transfer of thermal anomalies across the boundary, making it more likely thermal anomalies are continuous across the discontinuity.

[64] Lateral variation of intrinsic attenuation could result in variation of the observed amplitudes of seismic phases. As the discontinuity reflection is always compared to the surface reflected phase, only attenuation between the discontinuity and surface reflection point will contribute to variations in precursor reflection amplitudes. However, given the long wavelength nature of our data, attenuation of the reference pulse is not likely to be a significant factor in determination precursor amplitudes [e.g., see *Neele and Snieder*, 1992].

[65] The presence of an anisotropic material adjacent to the 410-km discontinuity, with a varying orientation for the fast axis could also cause precursor amplitude variations. Anisotropic effects are generally more pronounced for *S* waves than for *P* waves, so this could explain the greater variability observed in *S*410*S* amplitudes compared to *P*410*P*. However, the details of reflection coefficients in anisotropic media are complex, and a full discussion is beyond the scope of this study.

[66] *Bercovici and Karato* [2003] have speculated that upwelling material passing through the 410-km discontinuity could undergo dehydration-induced partial melting. Both *Revenaugh and Sipkin* [1994b] and *Song et al.* [2004] have observed regional zones of low-velocity zones above the 410-km discontinuity, and they interpreted them as regions where partial melt exists atop the 410-km discontinuity. If this occurs globally, then we would expect that regions of high-reflection coefficient correspond to regions with a larger degree of partial melting above the discontinuity. However, there is a complication as the associated water content beneath the discontinuity would also lower the seismic velocities in wadsleyite. The presence of partial

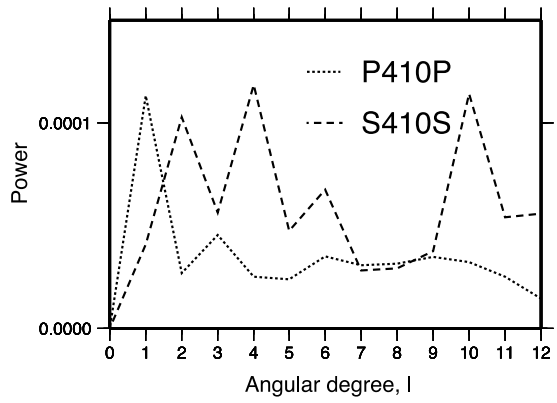

Figure 11. Amplitude spectra (average power per angular degree, *l*) for the spherical harmonic expansions of *P*410*P* and *S*410*S* amplitudes. The inner product of the spherical harmonics is normalized to 1. The *P*410*P* spectra is dominated by a degree-1 signature while the *S*410*S* is dominated by shorter-wavelength signals at degrees 4 and 10.

melt would be expected to affect *S* wave velocities more than *P* waves. Hence it may be that the short wavelengths in *S* wave reflection coefficient that we observe are due to short-wavelength variations in a melt layer, while the *P* wave variations are primarily sensitive to another process.

6. Conclusions

[67] We have examined the amplitude of *P* and *S* waves reflected from the 410-km discontinuity. We find that *P*410*P* amplitudes are regionally variable, being lower under North America and China, and higher beneath the North Pacific. The *S* wave reflection amplitudes show less variability on a regional scale. However, when smaller areas are considered, we find that *S*410*S* amplitudes vary but over shorter spatial lengths than for *P*410*P* amplitudes.

[68] The lack of correlation between our *P*410*P* and *S*410*S* reflection amplitudes could be due to the presence of melt, water, or other chemical heterogeneities in the upper mantle and transition zone. Other factors such as temperature, mantle olivine content variations, or focusing from mantle structure would require *P*410*P* and *S*410*S* amplitudes to correlate and so cannot explain all the variation.

[69] The reflection amplitudes constrain the global average and regional impedance contrasts across the 410-km discontinuity. Our values for the impedance contrast at 410 km appear to be more consistent with a low-olivine piclogite model for mantle composition. However, this assumes an anhydrous wadsleyite phase. A high-olivine pyrolite mantle could be consistent with our impedance contrasts if hydration of the wadsleyite phase is taken into account.

[70] **Acknowledgments.** We would like to thank George Helffrich and Ray Chambers for their advice on the iterative deconvolution and bootstrap resampling techniques. We also thank Frederik Simons, Jeff Gu, and Henneke Paulssen for their constructive reviews of the manuscript. K.C. was supported under the NERC studentship grant NER/S/A/2002/10529. Seismic data were generated by the IRIS/IDA/USGS networks, and the Oxford data facility is supported by NERC grant NER/F/S/2001/00369.

References

Aki, K., and P. G. Richards (1980), *Quantitative Seismology*, W. H. Freeman, New York.

Bercovici, D., and S. Karato (2003), Whole-mantle convection and the transition-zone water filter, *Nature*, *425*, 39–44.

Bona, M. D., and J. Boatwright (1991), Single station deconvolution of seismograms for subevent time histories, *Geophys. J. Int.*, *105*, 103–117.

Chapman, C. H. (1978), A new method for computing synthetic seismograms, *Geophys. J. R. Astron. Soc.*, *54*, 481–518.

Deuss, A., and J. H. Woodhouse (2001), Seismic observations of splitting of the mid-transition zone discontinuity in the Earth's mantle, *Science*, *294*, 354–357.

Deuss, A., and J. H. Woodhouse (2002), A systematic search for mantle discontinuities using *SS*-precursors, *Geophys. Res. Lett.*, *29*(8), 1249, doi:10.1029/2002GL014768.

Dziewonski, A. M., and D. L. Anderson (1981), Preliminary reference Earth model, *Phys. Earth Planet. Inter.*, *25*, 297–356.

Efron, B., and R. Tibshirani (1991), Statistical data analysis in the computer age, *Science*, *253*, 390–395.

Estabrook, C. H., and R. Kind (1996), The nature of the 660-kilometer upper-mantle seismic discontinuity from precursors to the *PP* phase, *Science*, *274*, 1179–1182.

Flanagan, M. P., and P. M. Shearer (1998), Global mapping of topography on transition zone velocity discontinuities by stacking SS precursors, *J. Geophys. Res.*, *103*, 2673–2692.

Flanagan, M. P., and P. M. Shearer (1999), A map of the topography on the 410-km discontinuity from *PP* precursors, *Geophys. Res. Lett.*, *26*, 549–552.

Gaherty, J. B., Y. Wang, T. H. Jordan, and D. J. Weidner (1999), Testing plausible upper mantle compositions using fine-scale models of the 410-km discontinuity, *Geophys. Res. Lett.*, *26*, 1641–1644.

Gossler, J., and R. Kind (1996), Seismic evidence for very deep roots of continents, *Earth Planet. Sci. Lett.*, *138*, 1–13.

Gu, Y., A. M. Dziewonski, and C. B. Agee (1998), Global de-correlation of the topography of transition zone discontinuities, *Earth Planet. Sci. Lett.*, *157*, 57–76.

Helffrich, G. R. (2000), Topography of the transition zone discontinuities, *Rev. Geophys.*, *38*, 141–158.

Helffrich, G. R., and B. J. Wood (1996), 410-km discontinuity sharpness and the form of the olivine $\alpha - \beta$ phase diagram: Resolution of apparent seismic contradictions, *Geophys. J. Int.*, *126*, F7–F12.

Jacobsen, S. D., J. R. Smyth, H. Spetzler, C. M. Holl, and D. J. Frost (2004), Sound velocities of iron-bearing hydrous ringwoodite, *Phys. Earth Planet. Inter.*, *143–144*, 47–56, doi:10.1016/j.pepi.2003.07.19.

Kikuchi, M., and H. Kanamori (1982), Inversion of complex body waves, *Bull. Seismol. Soc. Am.*, *72*, 491–506.

Menke, W. (1989), *Geophysical Data Analysis: Discrete Inverse Theory*, Springer, New York.

Mooney, W. D., G. Laske, and G. Masters (1998), A new global crustal model at 5 × 5 degrees: CRUST5.1, *J. Geophys. Res.*, *103*, 727–747.

Neele, F., and R. Snieder (1992), Topography of the 400 km discontinuity from the observations of long period $P_{400}P$ phases, *Geophys. J. Int.*, *109*, 670–682.

Neele, F., H. de Regt, and J. VanDecar (1997), Gross errors in upper mantle discontinuity topography from underside reflection data, *Geophys. J. Int.*, *129*, 194–204.

National Oceanic and Atmospheric Administration (NOAA) (1988), Etopo-5 bathymetry/topography data, *Data Announc. 88-mgg-02*.

Revenaugh, J., and T. H. Jordan (1991), Mantle layering from *ScS* reverberations 2. The transition zone, *J. Geophys. Res.*, *96*, 19,763–19,780.

Revenaugh, J., and S. A. Sipkin (1994a), Mantle discontinuity structure beneath China, *J. Geophys. Res.*, *99*, 21,911–21,927.

Revenaugh, J., and S. A. Sipkin (1994b), Seismic evidence for silicate melt atop the 410-km discontinuity, *Nature*, *369*, 474–476.

Ritsema, J., H. J. van Heijst, and J. H. Woodhouse (1999), Complex shear wave velocity structure imaged beneath Africa and Iceland, *Science*, *286*, 1925–1928.

Rost, S., and M. Weber (2002), The upper mantle transition zone discontinuities in the Pacific as determined by short-period array data, *Earth Planet. Sci. Lett.*, *204*, 347–361.

Shearer, P. (1996), Transition zone velocity gradients and the 520-km discontinuity, *J. Geophys. Res.*, *101*, 3053–3066.

Shearer, P., and M. Flanagan (1999), Seismic velocity and density jumps across the 410- and 660-kilometer discontinuities, *Science*, *285*, 1545–1548.

Shearer, P. M. (1993), Global mapping of upper mantle reflectors from long-period SS precursors, *Geophys. J. Int.*, *115*, 878–904.

Song, T. A., D. V. Helmberger, and S. P. Grand (2004), Low velocity zone atop the 410-km discontinuity in the northwestern United States, *Nature*, *427*, 530–533.

Stixrude, L. (1997), Structure and sharpness of phase transitions and mantle discontinuities, *J. Geophys. Res.*, *102*, 14,835–14,852.

van der Meijde, M., F. Marone, D. Giardini, and S. van der Lee (2003), Seismic evidence for water deep in the Earth's upper mantle, *Science*, *300*, 1556–1558.

Vidale, J. E., and H. M. Benz (1992), Upper-mantle seismic discontinuities and the thermal structure of subduction zones, *Nature*, *356*, 678–683.

Weidner, D. J., and Y. Wang (2000), Phase transformations: Implications for mantle structure, in *Earth's Deep Interior: Mineral Physics and Tomography From the Atomic to the Global Scale*, *Geophys. Monogr. Ser.*, vol. 117, edited by S. Karato et al., pp. 215–235, AGU, Washington, D. C.

Wood, B. J. (1995), The effect of H_2O on the 410-kilometer seismic discontinuity, *Science*, *268*, 74–76.

Yusa, H., and T. Inoue (1997), Compressibility of hydrous wadsleyite (β-phase) in Mg_2SiO_4 by high pressure X-ray diffraction, *Geophys. Res. Lett.*, *24*, 831–834.

K. Chambers and J. H. Woodhouse, Department of Earth Sciences, University of Oxford, Parks Road, Oxford OX1 3PR, UK. (kit.chambers@earth.ox.ac.uk; john.woodhouse@earth.ox.ac.uk)

A. Deuss, Institute of Theoretical Geophysics, Department of Earth Sciences, University of Cambridge, Madingley Road, Cambridge CB3 0EZ, UK. (deuss@esc.cam.ac.uk)